

Reversal magnetization, spin reorientation, and exchange bias in YCrO_3 doped with praseodymiumA. Durán,^{1,*} R. Escamilla,² R. Escudero,² F. Morales,² and E. Verdín³¹*Universidad Nacional Autónoma de México, Centro de Nanociencias y Nanotecnología, Km. 107 Carretera Tijuana-Ensenada, Apartado Postal 14, C. P. 22800, Ensenada, B. C., México*²*Universidad Nacional Autónoma de México, Instituto de Investigaciones en Materiales, Apartado Postal 70-360, Ciudad de México 04510, México*³*Universidad de Sonora, Departamento de Física, Apartado Postal 1626, Hermosillo, Sonora, México*

(Received 15 February 2017; revised manuscript received 4 October 2017; published 16 January 2018)

Crystal structure, thermal properties, and magnetic properties were studied systematically in $\text{Y}_{1-x}\text{Pr}_x\text{CrO}_3$ with $0.0 \leq x \leq 0.3$ compositions. Magnetic susceptibility and specific-heat measurements show an increase in the antiferromagnetic transition temperature (T_N) as Pr is substituted in the Y sites and notable magnetic features are observed below T_N . Strong coupling between magnetic and crystalline parameters is observed in a small range of Pr compositions. A small perturbation in the lattice parameters by a Pr ion is sufficient to induce a spin-reorientation transition followed by magnetization reversal to finally induce the exchange-bias effect. The spin-reorientation temperature (T_{SR}) is increased from 35 to 149 K for $0.025 \leq x \leq 0.1$ compositions. It is found that the Cr spin sublattice rotates continuously from T_{SR} to a new spin configuration at lower temperature. In addition, magnetization reversal is observed at $T^* \sim 35$ K for $x = 0.05$ up to $T^* \sim 63$ K for $x = 0.20$ composition. The M - H curves show a negative exchange-bias effect induced by Pr ions, which are observed below 100 K and are more intense at 5 K. At 10 K, the magnetic contribution of the specific heat as well as the ZFC magnetization show the rise of a peak with increasing Pr content. The magnetic anomaly could be associated with the freezing of the Pr magnetic moment randomly distributed at the $4c$ crystallographic site. A clear correspondence between spin reorientation, magnetization reversal, and exchange-bias anisotropy with the tilting and octahedral distortion is also discussed.

DOI: [10.1103/PhysRevMaterials.2.014409](https://doi.org/10.1103/PhysRevMaterials.2.014409)**I. INTRODUCTION**

Complex oxides of transition metals with perovskite structure represent a fascinating playground for basic solid-state research: new electronics and exotic ground states emerge via the competing interplay between spin, orbital, charge, and lattice degrees of freedom [1]. High- T_c superconductivity, colossal magnetoresistance, coexistence and competition of magnetism, and ferroelectricity are perhaps the best known examples. Recently, there has been a renewed interest in rare-earth manganites, ferrites, orthoferrites, and orthochromites due to the coexistence or coupling between lattice and magnetic order parameters leading to the magnetoelectric effect and striking/exotic magnetic properties [2–6]. In these compounds, from a basic point of view, a growing interest has been focused on the microscopic interactions responsible for the interplay between lattice and spin ground states [7]. This phenomenon is associated with a technologically appealing potential for applications as magneto-optic, spintronic, and data storage devices [8–10]. From a general point of view, the orthochromites with the formula $R\text{CrO}_3$, where $R = \text{Y}$ or a rare earth, are isostructural orthorhombic perovskite-derived structures (space group $Pbnm$). The R substitution from La to Lu decreases the tolerance factor, causing cooperative octa-

hedral rotation, and consequently the CrO_6 octahedral tilting is progressively reduced. Accordingly, the antiferromagnetic order (AFM) temperature of the Cr^{+3} sublattice is decreased from 282 K for LaCrO_3 to 112 K for LuCrO_3 [11]. Below the Néel temperature T_N , these compounds present a weak ferromagnetism (WFM) arising from a slight canting of the AFM spins that lie either along the a or c axis of the unit cell [12]. The WFM results from an antisymmetric superexchange between Cr^{+3} spins, also known as the Dzyaloshinskii-Moriya (DM) interaction [13,14]. The DM exchange interaction is the primary reason for the coupling of the spin and lattice degrees of freedom [3]. Interestingly, when the crystal contains both a d -ion subsystem and an f -ion subsystem, the DM interaction breaks the inversion symmetry through incommensurate magnetization on the d -ion subsystem at T_N [15]. On the other hand, the magnetic behavior becomes more complex as the magnetization of the f -ion subsystem increases below T_N . Accordingly, a rich variety of magnetic and electric properties, such as magnetostriction-induced polarization, spin reorientation, magnetization reversal, and exchange bias, is reported in several orthorhombic manganites, orthochromites, and orthoferrites [3,6,15]. Different combinations of rare-earth and transition-metal ions, including a relative concentration between them, can produce ferroelectric polarization at the magnetic ordering and a characteristic behavior called magnetization reversal (MR). MR means that the magnetization leads to a diamagnetic state at a certain temperature (compensation temperature, T^*) under a low applied magnetic

*Author to whom all correspondence should be addressed: dural@cny.unam.mx

field [16–18]. This phenomenon is not exclusive to these compounds; rather, it is present in a larger group of materials such as spinels, garnets, orthovanadates, and Prussian blue analogs [19–22]. Magnetoreversal behavior can be explained using the Néel criterion; however, for others such as YVO_3 the competition between the DM interaction and single-ion magnetic anisotropy (SIMA) has been suggested as the most viable explanation [23,24]. The MR in orthochromites is a clear manifestation that the magnetic ground states are unstable and susceptible to small perturbations caused by the strong competition between f -ion and d -ion subsystems and by octahedral tilting arising from the R partial substitution. This last aspect has been addressed only slightly in recent research on these phenomena.

In this paper, we provide a detailed study of the structural, thermal, and magnetic properties of the $\text{Y}_{1-x}\text{Pr}_x\text{CrO}_3$ solid solution. The structural and magnetic measurements indicate that the Pr substitution has a notable effect on the magnetic ground state. Spin reorientation (SR) and reversal magnetization are very sensitive to Pr substitution in a narrow range of Pr composition. These facts suggest not only an energetic condition for the presence of SR and MR but also the development of ferromagnetic domains coexisting with antiferromagnetic domains, which lead to the development of exchange magnetic anisotropy, also called exchange bias (EB). The close connection between octahedral distortion and these complex magnetic ground states is analyzed and discussed.

II. EXPERIMENTAL DETAILS

The self-propagating high-temperature synthesis (combustion) method was used to produce polycrystalline $\text{Y}_{1-x}\text{Pr}_x\text{CrO}_3$ with $0.0 \leq x \leq 0.3$ solid solution samples. Stoichiometric amounts of precursor nitrates $\text{Y}(\text{NO}_3)_3 \cdot 6\text{H}_2\text{O}$ (99.8% Alfa-Aesar), $\text{Pr}(\text{NO}_3)_3 \cdot 6\text{H}_2\text{O}$ (99.9% Alfa-Aesar), and $\text{Cr}(\text{NO}_3)_3 \cdot 9\text{H}_2\text{O}$ (99.9% Sigma-Aldrich) were dissolved in 2-methoxyethanol as a carburant and distilled water to form the precursor solution. The synthesis details were reported in Ref. [25]. The fine as-combustion powders were then ground and thermally treated in a furnace in a single-step process: a heating rate of $10^\circ\text{C min}^{-1}$ to reach 1200°C for 6 h. Phase identification of the samples was done with an x-ray Siemens D5000 diffractometer using $\text{Co } K\alpha$ radiation and a Fe filter. Intensities were measured at room temperature in steps of 0.02° , for 14 s, in the 2θ range 10° – 100° . The crystallographic phases were identified by comparison with the x-ray patterns of the JCPDS database. The crystallographic parameters were determined using a Rietveld refinement program, MAUD v 1.7.7 (Ref. [26]) with multiphase capability. The specific-heat measurements were carried out on the PPMS (Physical Property Measurement System, Quantum Design) at temperatures from 2 to 300 K. Magnetization was measured with a SQUID-based magnetometer (MPMS-5T by Quantum Design). The susceptibility measurements were performed at 1 kOe in the zero-field-cooled (ZFC) and field-cooled (FC) modes (2–300 K) while the magnetization versus applied magnetic-field measurements were performed at $\pm 5\text{ T}$ at 5, 50, and 100 K.

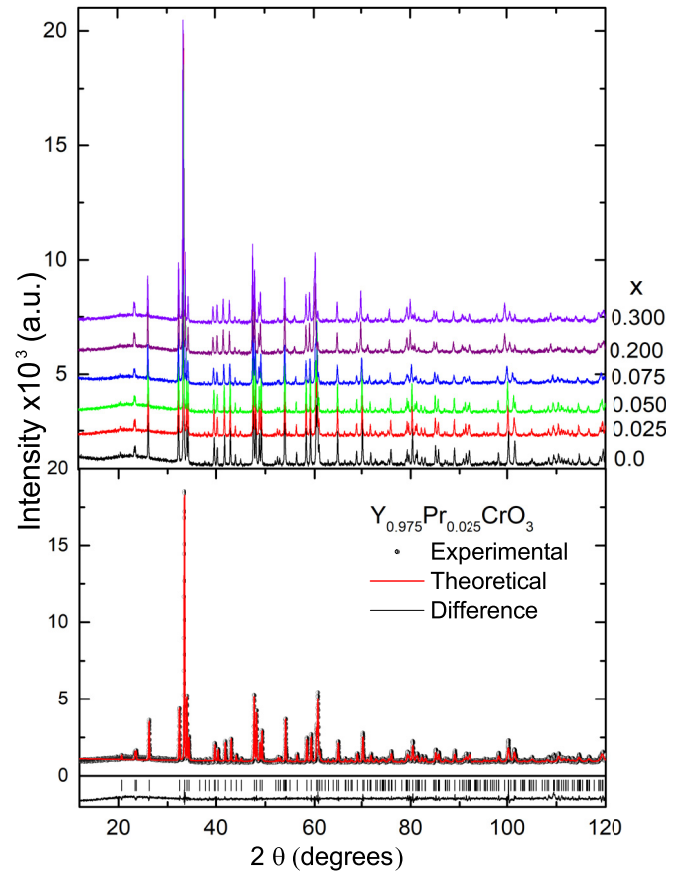


FIG. 1. Upper panel: x-ray diffraction patterns for $\text{Y}_{1-x}\text{Pr}_x\text{CrO}_3$ with $0.0 \leq x \leq 0.3$ compositions. The inset shows the shift of the plane (202), (040), (230), and (212) as Pr content. Bottom panel: the fitting results of the Rietveld analysis for the $x = 0.025$ sample along with experimental results (\bullet) and calculated results ($—$), and the bottom line denotes the difference between the observed and calculated patterns.

III. RESULTS

A. Structural analysis

Figure 1 shows the x-ray powder-diffraction patterns for $\text{Y}_{1-x}\text{Pr}_x\text{CrO}_3$ with $0.0 \leq x \leq 0.3$ compositions. The analysis of the data shows a single phase for all samples corresponding to the distorted perovskite structure with orthorhombic symmetry YCrO_3 (ICSD no. 34-0365). The x-ray-diffraction patterns of the samples were Rietveld-fitted using a space group $Pbnm$ (No. 62), considering the possibility that Pr occupies Y sites. As an example, the profile fitting of the x-ray-diffraction pattern for the $\text{Y}_{0.975}\text{Pr}_{0.025}\text{CrO}_3$ sample is shown in the bottom panel of Fig. 1. The crystallographic parameters obtained from the Rietveld refinements are shown in Table I. From the refinement results, the lattice parameters and the unit-cell volume behavior with Pr content are seen in Fig. 2. For the undoped sample, the lattice parameter values are in agreement with other published results [11,25]. The a and c axes show a significant increase with increasing Pr content, while the b axis shows a slight decrease. The net result is an increase in cell volume with increasing Pr content, which is due to the effective ionic radius of Pr^{+3} (1.126 \AA) being larger than that

TABLE I. Structural parameters and atomic positions for the $(Y_{1-x}Pr_x)CrO_3$ system at room temperature.

$x =$		0.00	0.025	0.050	0.075	0.100	0.200	0.300
a (Å)		5.2426(1)	5.2487(1)	5.2525(1)	5.2630(1)	5.2628(2)	5.2829(1)	5.3052(1)
b (Å)		5.5237(1)	5.5241(1)	5.5224(1)	5.5249(1)	5.5208(2)	5.5180(1)	5.5146(1)
c (Å)		7.5344(1)	7.5407(1)	7.5436(1)	7.5550(2)	7.5531(3)	7.5716(1)	7.5923(1)
V (Å ³)		218.19	218.64	218.81	219.68	219.45	220.72	222.12
Y	X	-0.0169(4)	-0.0172(3)	-0.0176(3)	-0.0178(2)	-0.0182(3)	-0.0195(3)	-0.0208(3)
	Y	0.0664(2)	0.0655(2)	0.0647(1)	0.0639(1)	0.0630(2)	0.0596(2)	0.0562(2)
	B (Å ²)	0.13(3)	0.17(4)	0.10(2)	0.17(3)	0.31(4)	0.39(5)	0.37(2)
Cr	B (Å ²)	0.11(4)	0.14(3)	0.10(3)	0.16(5)	0.26(3)	0.26(3)	0.29(1)
	O(1)	X	0.099(2)	0.099(1)	0.100(2)	0.101(1)	0.102(2)	0.105(2)
O(1)	Y	0.464(2)	0.464(1)	0.465(1)	0.465(2)	0.465(1)	0.466(1)	0.467(1)
	B (Å ²)	0.25(3)	0.39(1)	0.25(2)	0.25(2)	0.46(3)	0.20(3)	0.25(3)
	O(2)	x	-0.306(1)	-0.306(1)	-0.305(1)	-0.305(1)	-0.304(1)	-0.303(2)
O(2)	y	0.306(1)	0.306(1)	0.305(1)	0.305(2)	0.305(1)	0.303(1)	0.302(1)
	z	0.056(1)	0.056(1)	0.055(1)	0.055(1)	0.054(1)	0.053(1)	0.051(1)
	B (Å ²)	0.27(2)	0.37(2)	0.20(1)	0.19(2)	0.25(3)	0.29(5)	0.19(2)
	R_b (%)	3.9	3.8	4.3	4.0	3.7	3.6	3.6
	R_{wp} (%)	5.1	5.1	5.7	5.1	4.9	4.6	4.5
	R_{exp} (%)	2.8	3.0	3.1	3.1	3.0	2.9	2.9
	χ^2 (%)	1.8	1.7	1.8	1.6	1.6	1.6	1.6

Note: Space group: $Pbnm$. Atomic positions: Y, $4c$ ($x, y, 0.25$); Cr, $4b$ ($0, 0.5, 0$); O(1), $4c$ ($x, y, 0.25$); and O(2), $8d$ (x, y, z).

of the Y^{+3} (1.019 Å) ion with eight-coordination [27]. Note that the lattice parameters and the volume reveal a small anomaly at about $x = 0.075$ of Pr content. This behavior appears to be inconsistent under the criterion of the chemical pressure

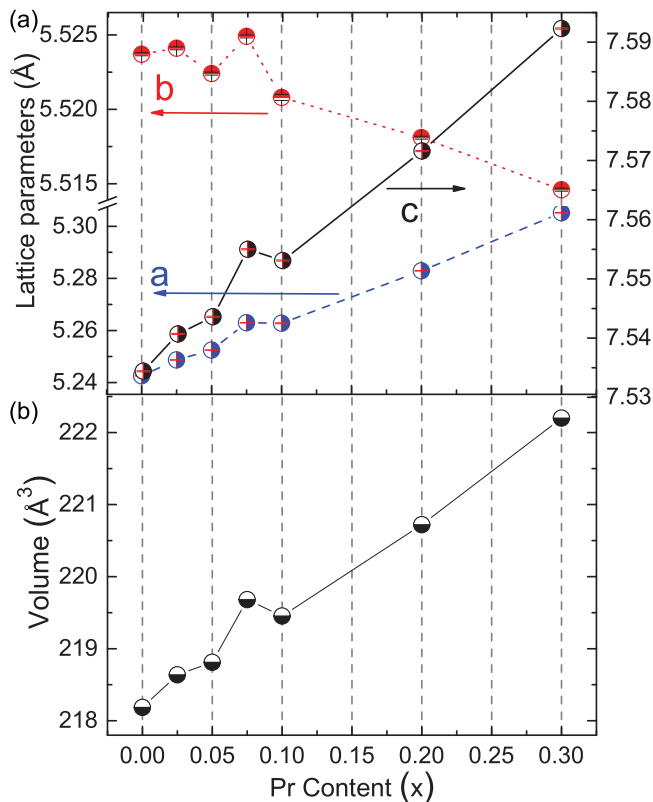


FIG. 2. (a) Lattice parameters are in Å on both y axes, and (b) shows the unit-cell volume of the orthorhombic structure as a function of Pr content.

effect. Thus, to get a more precise understanding of this behavior, the internal crystallographic parameters (octahedral distortion, bond length, bond angle, and tilting) were extracted from the Rietveld refinement and are listed in Table II. The internal structural parameters, such as the octahedral distortion (Δ) and the Cr-O-Cr bond angles, are affected by the Y/Pr substitution, whereas the average $\langle Cr-O \rangle$ bond lengths are rigid and remain almost constant. This fact is an expected result for Cr^{+3} in an octahedral environment [28,29]. The Cr-O-Cr angles along the [001] and [110] direction correspond to the in-phase octahedral tiltings α_x^+ and antiphase octahedral tilting $\alpha_x^- = \alpha_y^-$, respectively, as is seen in Figs. 3(a) and 3(b). There, the apical oxygen atoms are denoted as O(1) and the equatorial oxygen atoms as O(2) in the CrO_6 octahedral perovskite. Both octahedral tiltings can be calculated using the expressions $\theta = [180 - \langle Cr-O(1)-Cr \rangle]/2$ and $\cos \phi = \cos\{[180 - \langle Cr-O(2)-Cr \rangle]/2\}/\sqrt{\cos \theta}$ [30]. Here, the tilt angles ϕ [001] and θ [110] for $x = 0$ are in agreement with the values reported in Refs. [11,31]. Figures 3(c) and 3(d) show an increase in the tilt θ angle and a decrease in the tilt ϕ angle upon increasing the Pr content. Concomitantly, the continuous deviation of the in-phase and antiphase tilting angles and the octahedral distortion with Y/Pr substitution should have a strong influence on the magnetic properties, as will be discussed in what follows.

B. Magnetic results

1. Antiferromagnetic regime

The temperature dependence of the ZFC and FC magnetic susceptibility under an applied field of 1 kOe for all samples ($0.0 \leq x \leq 0.3$) is shown in Fig. 4. Note that the Y/Pr substitution gives rise to a striking and unusual development in the magnetic ground states. For $x = 0$, the susceptibility shows a large splitting in the ZFC and FC curves below ~ 142 K [see the

TABLE II. Geometrical parameters characterizing the crystal structure of the $(Y_{1-x}Pr_x)CrO_3$ system. The octahedral distortion parameter Δ of a coordination polyhedron BO_N with an average bond length $B-O$ (d) is defined as $\Delta = (1/N)\sum_{n=1,N}\{(d_n - \langle d \rangle)/\langle d \rangle\}^2$ (Ref. [59]). The tilt angles φ and θ of CrO_6 octahedral around the pseudocubic [001] and [110] directions are obtained from the two angles θ_1 and θ_2 (Ref. [30]).

$x =$	0.000	0.025	0.050	0.075	0.100	0.200	0.300
Cr-O1:2	1.964(3)	1.966(2)	1.967(3)	1.972(2)	1.971(2)	1.976(3)	1.973(2)
Cr-O2:2	1.975(3)	1.977(3)	1.974(2)	1.977(3)	1.973(3)	1.981(3)	1.987(3)
Cr-O2:2	2.017(2)	2.018(3)	2.015(3)	2.016(3)	2.016(3)	2.010(2)	2.010(2)
$\langle Cr - O2 \rangle$	1.996	1.997	1.995	1.996	1.995	1.996	1.999
$\langle Cr - O \rangle$	1.985	1.987	1.985	1.988	1.987	1.989	1.990
$\Delta(Cr - O) \times 10^{-4}$	2.64	2.53	2.27	1.96	2.18	1.13	1.17
$\theta_1: Cr - O(1) - Cr$	147.12(2)	147.11(2)	146.94(3)	146.66(2)	146.37(3)	145.62(3)	145.69(3)
$\theta_2: Cr - O(2) - Cr$	145.04(2)	145.03(3)	145.62(2)	145.61(3)	146.05(3)	146.77(3)	147.79(3)
φ [001]	13.11	13.11	12.66	12.57	12.16	11.36	10.62
θ [110]	16.44	16.44	16.53	16.67	16.81	17.19	17.16

inset of Fig. 4(a)]. It has been reported that the antiferromagnetic G -type structure with spin canting of the Cr^{+3} ($S = 3/2$) ion occurs below ~ 142 K for $YCrO_3$ [32]. The substitution of Pr at the Y site produces an increase of the T_N up to 166 K for $x = 0.30$. Moreover, the magnetic susceptibility curves show intriguing magnetic properties such as spin reorientation (SR) and temperature-induced reversal magnetization (MR) at $T^* < T_{SR} < T_N$. The susceptibility curves show a splitting of ZFC and FC mode followed by a sudden drop of the magnetization

at ~ 35 and ~ 105 K for $x = 0.025$ and 0.050 , respectively. This is a signature of the spin-reorientation transition occurring at T_{SR} . The hysteresis in the FC and ZFC magnetization data below SR suggests a first-order transition [arrows in Fig. 4(b)] in a similar way as was observed in the $YFe_{1-x}Mn_xO_3$ compound [33]. For higher Pr content, the T_{SR} is shifted to higher temperature from ~ 35 K for $x = 0.025$ to ~ 145 K for the $x = 0.10$ composition. Below T_{SR} , a characteristic

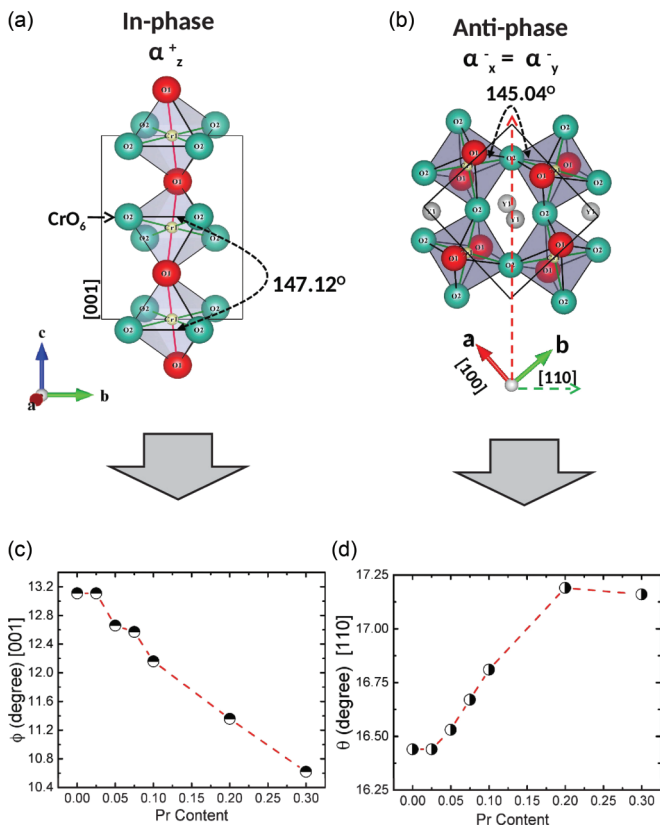


FIG. 3. Octahedral arrangement of the orthorhombic $Pbnm$ ($\alpha^- \alpha^+ \alpha^+$) phase of $Y_{1-x}Pr_xCrO_3$ perovskite. (a) In-phase α^+ and (b) antiphase $\alpha^- = \alpha^-$ tilting about the [001] and [110] axes of the CrO_6 polyhedron, respectively. The tilting angles along the [001] and [110] directions are also displayed in (c) and (d).

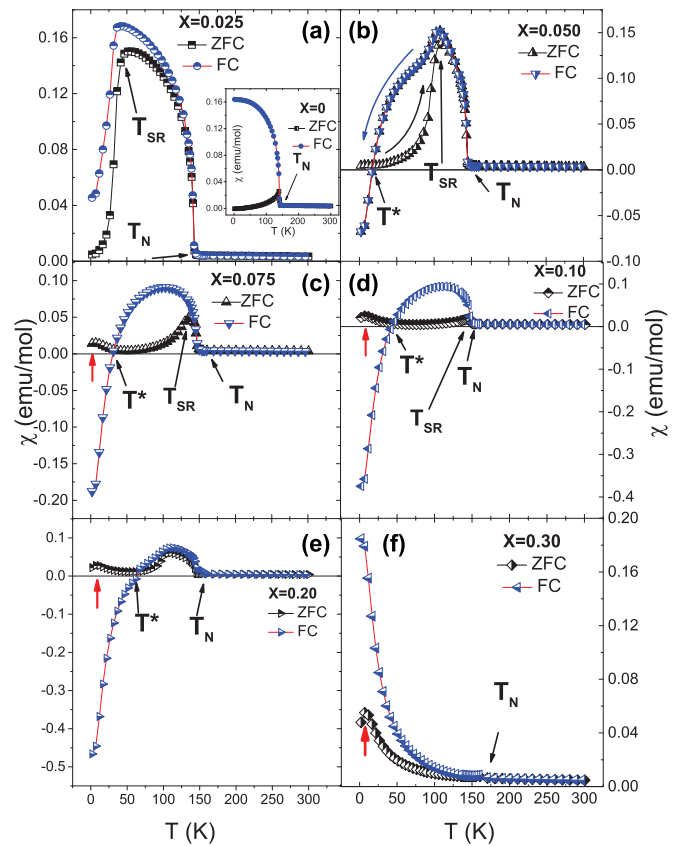


FIG. 4. Magnetic susceptibility and ZFC and FC cycles at 1 kOe from (a) $x = 0.025$ to (f) $x = 0.30$ compositions. In the panel graphs, T_N , T_{SR} , and T^* are the AFM transition, spin reorientation, and compensation temperatures, respectively. The inset of panel (a) shows the magnetic susceptibility for a pristine sample. The continuous line is a guide to the eye.

point in the FC curve is the negative magnetization or the induced MR at a relatively high applied magnetic field (1 kOe) in the $0.050 \leq x \leq 0.20$ composition range. Cooling in an applied field of 1 kOe, the magnetization shows a maximum with a positive magnetization, and magnetization reversal is observed at compensation temperatures (T^*) of 17, 31, 45, and 63 K for $x = 0.05, 0.075, 0.10,$ and 0.20 compositions to finally vanish for $x = 0.30$ of Pr content [Figs. 4(b)–4(d)]. The magnetization takes a value of about -0.5 emu/mol for $x = 0.2$ Pr content at 2 K. The negative magnetization value is similar to that obtained in the equimolar $\text{La}_{0.5}\text{Pr}_{0.5}\text{CrO}_3$, but in a weaker applied magnetic field (100 Oe) [16]. It is also noted that the magnetization reversal in $\text{Y}_{1-x}\text{Pr}_x\text{CrO}_3$ occurs in a narrower range of Pr content, between $0.050 \leq x \leq 0.2$, while the reversal magnetization in $\text{La}_{1-x}\text{Pr}_x\text{CrO}_3$ occurs in a broader range of composition ($0.2 \leq x \leq 0.8$) (Ref. [34]). At this point, a question that must be addressed is why both SR and MR phenomena occur in a narrow range of Pr composition ($0.025 \leq x \leq 0.20$). It is worth noting that in this narrow range of Pr compositions, an anomalous octahedral distortion occurs in close connection with the $t - e$ hybridization and magnetization behavior. These facts suggest not only the energy condition for the presence of both phenomena, but also the development of ferromagnetic domains coexisting with antiferromagnetic domains, which favor the development of the exchange bias effect at lower temperatures, as is indicated by the M - H curves in the following section.

2. M - H hysteresis loops

Magnetization as a function of the applied magnetic field (± 50 kOe) was measured at 5 K, after cooling from room temperature (through T_N) without an applied magnetic field for all compositions. Figure 5 shows the hysteresis loops for each composition measured at 5 K. As expected, the pristine sample shows a hysteresis loop due to spin-canting AFM ordering with the coercive field (H_c) and the remanent magnetization (M_r) of ± 16 kOe and $0.027 \mu_B/\text{f.u.}$ at 5 K, respectively [see the inset Fig. 5(a)], in agreement with the values reported in Refs. [25,35]. A drastic decrease of both H_c and M_r for $x = 0.025$ and 0.050 of Pr content is observed [Figs. 5(a) and 5(b)]. After that, the coercive field (H_c) increases and then decreases for $x = 0.075$ and 0.10 compositions, respectively. Finally, for the $x = 0.20$ and 0.30 compositions, H_c and M_r take values higher than the pristine sample. The result shows a strong ferromagnetic contribution for these last two compositions at 5 K. On the other hand, the M - H curves also show a shift of the hysteresis loop toward the negative applied field axis from $x = 0.025$ to 0.20 composition. This fact indicates exchange bias (EB) induced by Pr substitution. It is well known that the EB effects arise when the FM and AFM domains are coupled through an interface [6,36]. The results here suggest that both FM and AFM domains in close contact lead to an additional anisotropy (showed by asymmetric H_c) via exchange coupling in the bulk-doped samples. The negative shifting in the hysteresis curves is clearly seen from $x = 0.050$ to 0.10 Pr content at 5 K. For higher compositions, the EB tends to vanish. The behavior of the exchange-bias field H_{EB} , and the remanent magnetization M_{EB} , as a function of Pr content for 5, 50, and 100 K are plotted in Fig. 6. These values

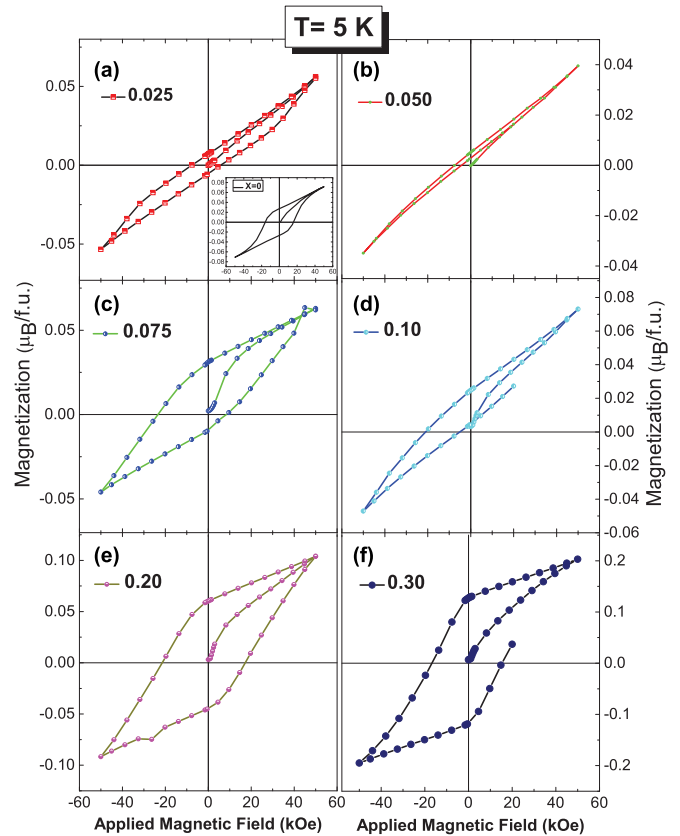


FIG. 5. M - H hysteresis loops measured at 5 K for $\text{Y}_{1-x}\text{Pr}_x\text{CrO}_3$ with $0 \leq x \leq 0.3$ solid solution. The inset of the upper panel shows the hysteresis loop for the pristine sample.

were determined for each concentration using the relation $H_{EB} = (H_+ + H_-)/2$ and $M_{EB} = (M_+ + M_-)/2$ taking the H and M values during ascending and descending branches of the hysteresis loops. At 5 K, the negative H_{EB} is near zero for $x = 0.05$ and continuously decreases down to ~ 0.13 kOe at $x = 0.10$; after that composition, the H_{EB} increases to almost vanish at $x = 0.30$ Pr content. In a similar way, the M_{EB} continuously increases with a maximum at $x = 0.10$ and then decreases for $x = 0.30$ of Pr content as seen in upper right panel of Fig. 6. Similarly, the M_{EB} and H_{EB} persist, but they are small at 50 K. H_{EB} and the M_{EB} are slightly increased for $x = 0.2$ and 0.3 . Finally, a turn from negative to positive H_{EB} is observed at about $x = 0.1$ at 100 K, as is shown in the lower panel of Fig. 6. It is worth noting that H_{EB} and M_{EB} display strong changes below T_{SR} and T^* with maximum values at $x = 0.10$ at 5 K. The competition of the FM and AFM domains, presumably due to Pr and the Cr interaction, are clearly appreciated at 5 K where Pr-O-Cr interactions become stronger. A maximum in H_{EB} and M_{EB} indicates that the canted AFM moments align with stronger intensity as opposed to the applied field giving rise to a negative exchange bias (NEB) [37] at $x = 0.1$.

3. Specific-heat measurements

Figure 7(a) shows the temperature dependence of total specific heat, C_p , for $\text{Y}_{1-x}\text{Pr}_x\text{CrO}_3$ with $x = 0.0, 0.05, 0.1, 0.2,$ and 0.3 from 300 down to 2 K. Two anomalies are observed

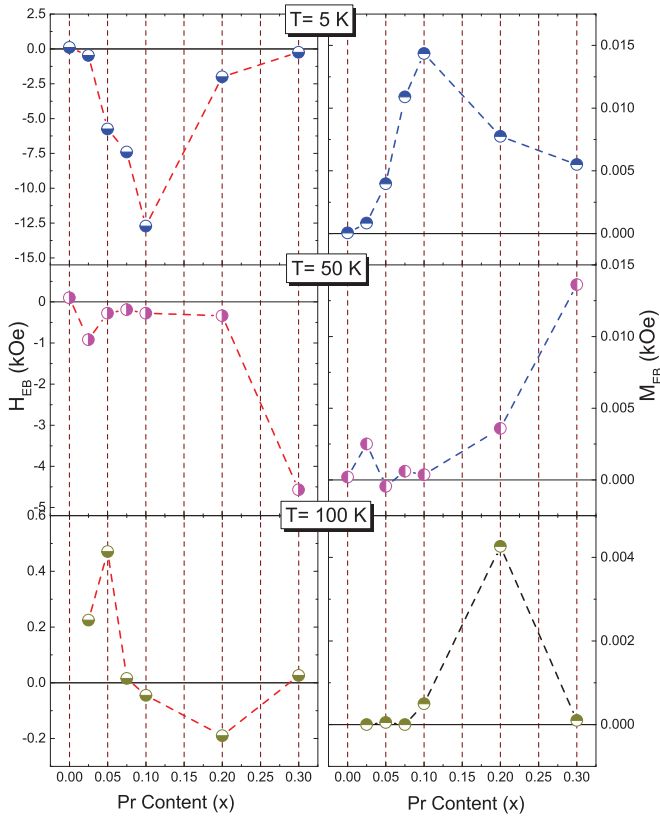


FIG. 6. H_{EB} and M_{EB} as a function of the Pr content at 5, 50, and 100 K.

in C_p , which are clearly observed in the expanded scale of the upper and lower inset of Fig. 7(a). The first anomaly occurs at T_N , which is indicative of the second-order AFM transition of the Cr ($d^3, S = 3/2$) magnetic moments. The upper inset shows an increase of AFM transition from 142 to 166 K in agreement with the magnetic measurement. The second anomaly is displayed at low temperature, as is seen in the lower inset of Fig. 7(a). The anomaly observed at about 10 K begins to increase with the Pr content to finish as a hump for $x = 0.3$. This feature resembles a Schottky anomaly. Figure 7(b) shows the C_p versus T curves from 30 down to 2 K for the $x = 0.3$ sample measured up to 9 T. There, the C_p versus T curve for the pristine sample is shown for comparison. Under an applied magnetic field, the hump is smoothed until it almost disappears at 9 T. The results ruled out the Schottky-like transition [38] induced by Pr substitution. On the contrary, the results clearly support that the magnetic anomaly at 10 K is associated with the Pr ions in the $YCrO_3$ matrix. To evaluate the magnetic contribution near T_N , the phonon contribution is estimated (and subtracted from the C_p) from the Debye formula,

$$C_{lat} = 9RN \left(\frac{T}{\theta_D} \right)^3 \int_0^{\theta_D/T} \frac{x^4 e^x}{(e^x - 1)^2} dx, \quad (1)$$

where $N = 5$ is the number of atoms per cell, $R = 8.314 \text{ J/mol K}$ is the ideal-gas constant, and θ_D is the Debye temperature. The Debye function reproduces the experimental data above 235 K with $T_D = 655 \text{ K}$. This function is shown as a continuous line in Fig. 8(a). There, the magnetic contribution

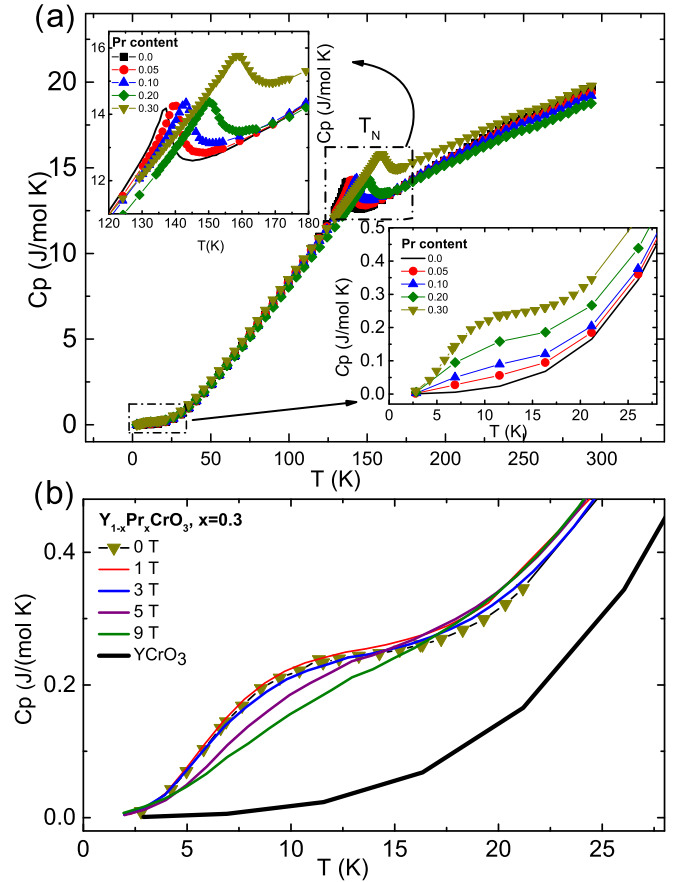


FIG. 7. (a) Temperature dependence of the specific heat C_p for the $Y_{1-x}Pr_xCrO_3$ solid solution. The upper and lower insets show an expanded scale around T_N and the development of an anomaly at about 10 K. (b) Specific heat for the $x = 0.3$ sample under an applied magnetic field up to 9 T. For comparison, the pristine sample is shown (thick line).

is also plotted as C_m/T for $YCrO_3$. The Debye temperature (Θ_D) values obtained for the different Pr concentrations are between 645 and 655 K. In Fig. 8(b) we plot the magnetic contribution, C_m/T , for $Y_{1-x}Pr_xCrO_3$ for $x = 0, 0.05, 0.10, 0.20,$ and 0.30 . The C_m/T shows that (i) the T_N anomaly shifts toward higher temperatures as x increases, in agreement with magnetic measurements; (ii) a broad peak at about 60 K, whose magnetic contribution increases slightly with increasing Pr content; and (iii) the arising of a peak at $\sim 10 \text{ K}$ with increasing Pr content. Recently, Sharma *et al.* [39] showed an additional phonon anomaly at 60 K likely related to the spin dynamic in the $YCrO_3$ compound. The large magnetic contribution was associated with the metastable spin-reorientation condition, which could be induced by an applied magnetic field at $\sim 60 \text{ K}$, as was reported by Jacobs *et al.* [40]. However, this assumption cannot be supported by our specific-heat results since the T_{SR} increases beyond 60 K with Pr content, as seen in Fig. 4. This fact ruled out the connection of spin reorientation with the anomaly at 60 K in C_m/T . On the other hand, the evolution of the peak at about 10 K [Fig. 8(b)], which only exists in $Y_{1-x}Pr_xCrO_3$, strongly suggest that it is related to the Pr-Pr exchange interaction, as was pointed out by Yamaguchi [41], which becomes visible at low temperature ($\sim 10 \text{ K}$).

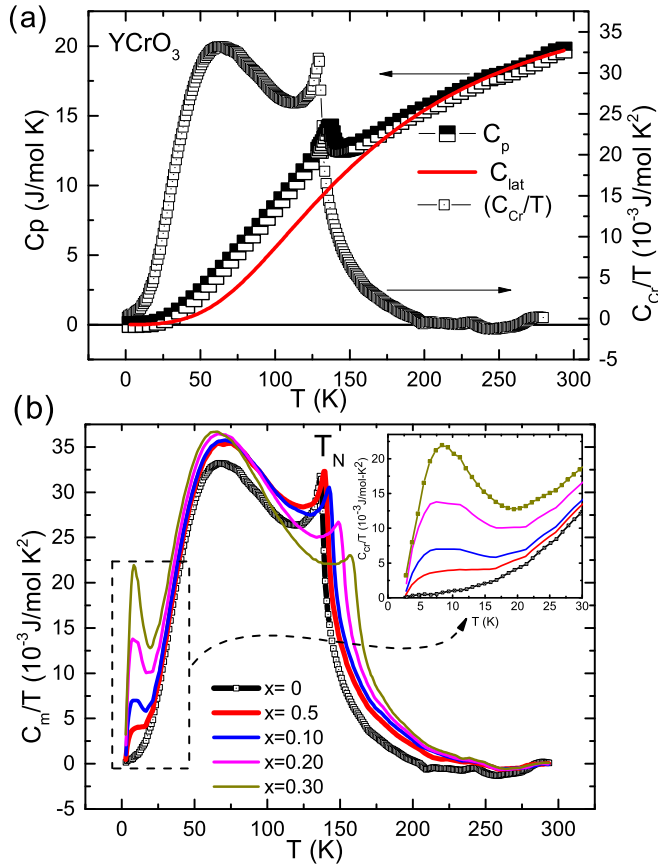


FIG. 8. (a) The fitting result (solid line) and experimental data (half-filled square) for $YCrO_3$ using the Debye specific-heat function. The magnetic contribution C_m/T is depicted with open squares. (b) The C_m/T is shown for $x = 0, 0.05, 0.1, 0.2$, and 0.3 compositions. The inset shows the development of the hump at about 10 K.

However, this assumption is not valid for diluted magnetic structure where the Pr ions are chemically disordered at the 4c crystallographic site.

IV. DISCUSSION

Experimental results reveal several changes in the magnetic properties induced by the partial substitution of Y by Pr ions. The unfilled f shell of Pr ions promotes the magnetic ground state toward more complex magnetic structures as a result of the anisotropic magnetic interactions of the Cr^{+3} ($S = 3/2$) and Pr^{+3} ($S = 1$) spins in the $Y_{1-x}Pr_xCrO_3$ ($0 \leq x \leq 0.3$) solid solution. The magnetic moments of the Cr^{+3} ions in the octahedral site are subjected to certain rotational forces arising through the exchange interaction between $Cr^{+3}-Cr^{+3}$, $Cr^{+3}-Pr^{+3}$, and the weaker $Pr^{+3}-Pr^{+3}$ exchange interaction. Under these conditions, the magnetic structure is controlled by the crystal symmetry. The first complex magnetic structure is the temperature-induced spin-reorientation transition with Pr doping. To discern the possible magnetic structure during the spin reorientation, the G -type AFM configuration according to Bertaut notation [42] as well as the experimental $M(H)$ curve are taken into account. The $RCrO_3$ family allows $\Gamma_1(A_x, G_y, C_z)$, $\Gamma_2(F_x, C_y, G_z)$, and $\Gamma_4(G_x, A_y, F_z)$ ground-

state configurations. The $\Gamma_4(G_x, A_y, F_z)$ ground state remains weakly ferromagnetic below T_N as it occurs with La and Y ions [5]. When the R ion is magnetic [43,44], not only is the $\Gamma_4(G_x, A_y, F_z)$ spin configuration possible but also the $\Gamma_1(A_x, G_y, C_z)$ and $\Gamma_2(F_x, C_y, G_z)$ spin configurations. The $\Gamma_2(F_x, C_y, G_z)$ configuration also presents weak ferromagnetism such as occurs in $TbCrO_3$, $HoCrO_3$, and $DyCrO_3$ compounds [41,45]. Contrary to this magnetic configuration, the $\Gamma_1(A_x, G_y, C_z)$ configuration does not allow weak ferromagnetism as it was reported in $ErCrO_3$, where $\Gamma_4(G_x, A_y, F_z)$ changes to the nonmagnetic $\Gamma_1(A_x, G_y, C_z)$ configuration below $T_{SR} \sim 22$ K [46,47]. In the present study, the induced spin-reorientation transition is shifted to higher temperatures upon Pr substitution [Figs. 4(a) and 4(b)], and experimentally it is seen as a sudden drop in the magnetization followed by a splitting of ZFC and FC magnetic susceptibility. For example, the T_{SR} increases from 35 to 105 K for $x = 0.025$ and 0.050. The results also show that the magnetic hysteresis loop diminishes for $x = 0.025$ concerning the pristine sample and almost disappears for $x = 0.050$ at 5 K, as is seen in Figs. 5(a) and 5(b). This magnetic behavior suggests that the Cr spin rotates from a weak ferromagnetic $\Gamma_4(G_x, A_y, F_z)$ to a nonmagnetic $\Gamma_1(A_x, G_y, C_z)$ configuration below T_{SR} . For $x = 0.025$, the reduced hysteresis loop suggests that the $\Gamma_1(A_x, G_y, C_z)$ configuration is incomplete at 5 K. For $x = 0.050$, the spin reorientation transition temperature is increased to 105 K and an almost pure collinear AFM phase is obtained, which is confirmed by the vanishing of the hysteresis loop at 5 K in Fig. 5(b); i.e., the $\Gamma_1(A_x, G_y, C_z)$ configuration is attained. The spin dynamic configuration as a function of temperature is more complex with higher Pr substitution, particularly at low temperatures since the $Pr^{+3} - O - Cr^{+3}$ magnetic interaction becomes important and may overcome the crystalline anisotropic forces. To provide a better understanding of the spin dynamic configuration for the $x = 0.075$ and 0.1 compositions, the inverse susceptibility data with the corresponding magnetic hysteresis loops at 5, 50, and 100 K are displayed in Figs. 9(a) and 9(b). For $x = 0.075$, the splitting of the ZFC and FC curves occurs at $T_{SR} \sim 138$ K, as seen in Fig. 9(a). The hysteresis loops at 100 K and the partial disappearance of the hysteresis at 50 K suggest that the Cr^{+3} spins rotate from $\Gamma_4(G_x, A_y, F_z)$ to an incomplete $\Gamma_1(A_x, G_y, C_z)$ configuration since an incipient hysteresis loop is observed at 50 K. It is possible that the complete $\Gamma_1(A_x, G_y, C_z)$ configuration could be attained just before $T^* \sim 36$ K [Fig. 9(a)], as is seen, for example, in Fig. 9(b) for $x = 0.10$ composition. There, T_{SR} increases up to ~ 145 K, and the hysteresis loop at 100 K and the subsequent vanishing at 50 K indicate that the spin reorientation changes from $\Gamma_4(G_x, A_y, F_z)$ to nonmagnetic $\Gamma_1(A_x, G_y, C_z)$ configuration at $T^* \sim 45$ K. The result also indicates that the easy axis of magnetization rotates beginning at T_{SR} and moving continuously with decreasing temperature, to finally finish at lower temperatures ($G_x \rightarrow G_y$), $T \sim T^*$.

According to Levison *et al.* [48], the easy axis either rotates continuously from T_{SR} down toward lower temperature (T_2) or jumps discontinuously with hysteresis effects. Yamaguchi [41] showed that the antisymmetric (DM) and the anisotropic-symmetric exchange interaction between M^{+3} and R^{+3} spins are responsible for both the rotational SR and the abrupt SR transition, generally occurring between T_N and the

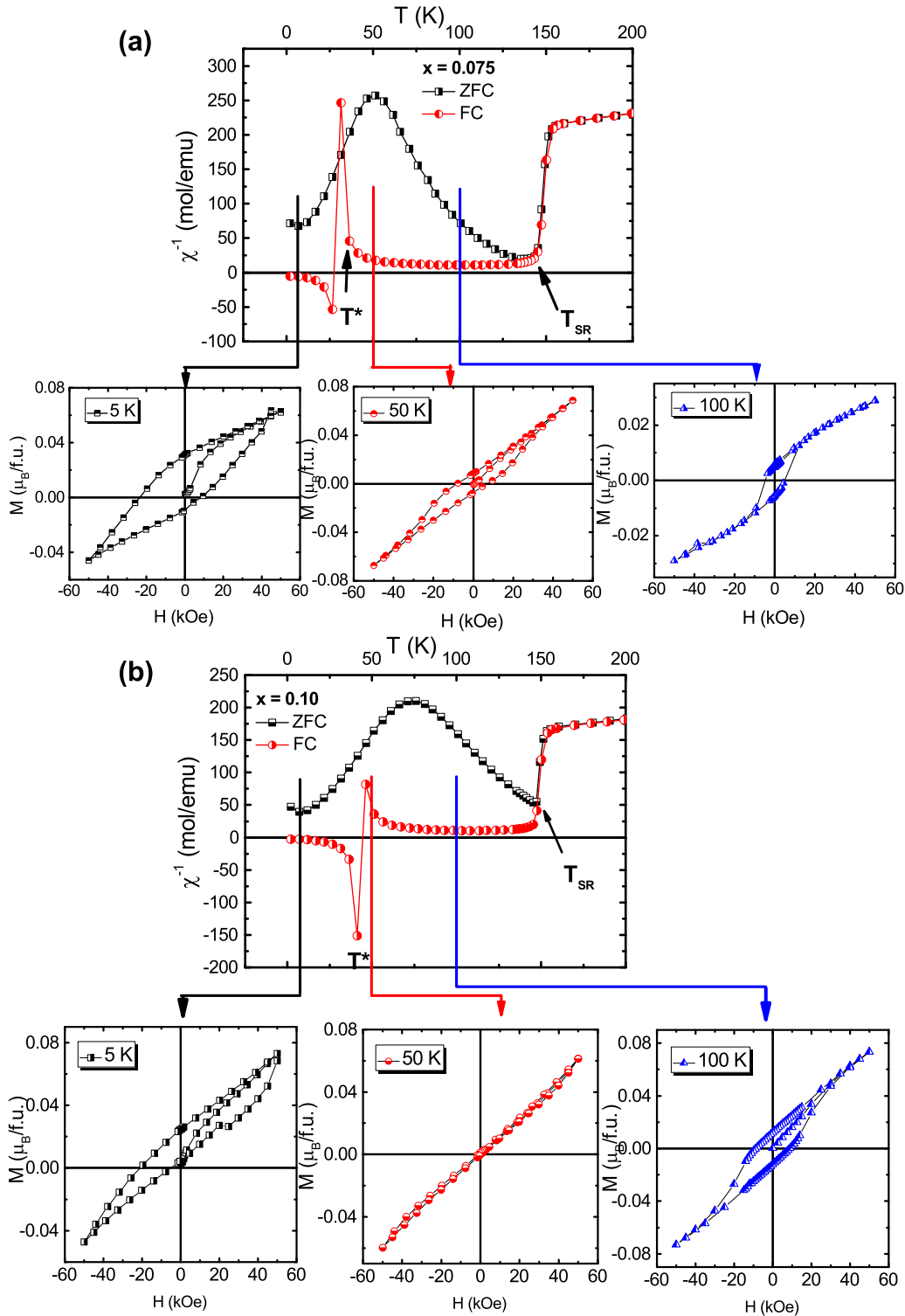


FIG. 9. The $\chi^{-1} - T$ data in the ZFC and FC mode along with the $M - H$ data at 5, 50, and 100 are shown for (a) $x = 0.075$ and (b) $x = 0.10$. T_{SR} indicates the temperature at which the spin reorientation occurs, and T^* is the compensation temperature.

magnetic transition of the R^{+3} sublattice. Note that the weak ferromagnetism vanishes into G_y -AFM ($F_z = 0$) when the magnetization reversal takes place at T^* , contrary to what happens in $NdCrO_3$ where a jump in the total specific heat confirms a first-order transition as a consequence of a sudden spin rotation at T_{SR} . The single anisotropic ion of Nd^{+3} is

responsible for the easy-axis rotation [38]. The abrupt spin rotation, in many cases, changes the reversal magnetization to positive magnetization values such as is observed in $GdCrO_3$ and $TmCrO_3$ compounds [49,50]. Two explanations of these results are plausible in $Y_{1-x}Pr_xCrO_3$ with $0.025 \leq x \leq 0.10$ composition: (i) the exchange interaction between Pr^{+3} - Cr^{+3}

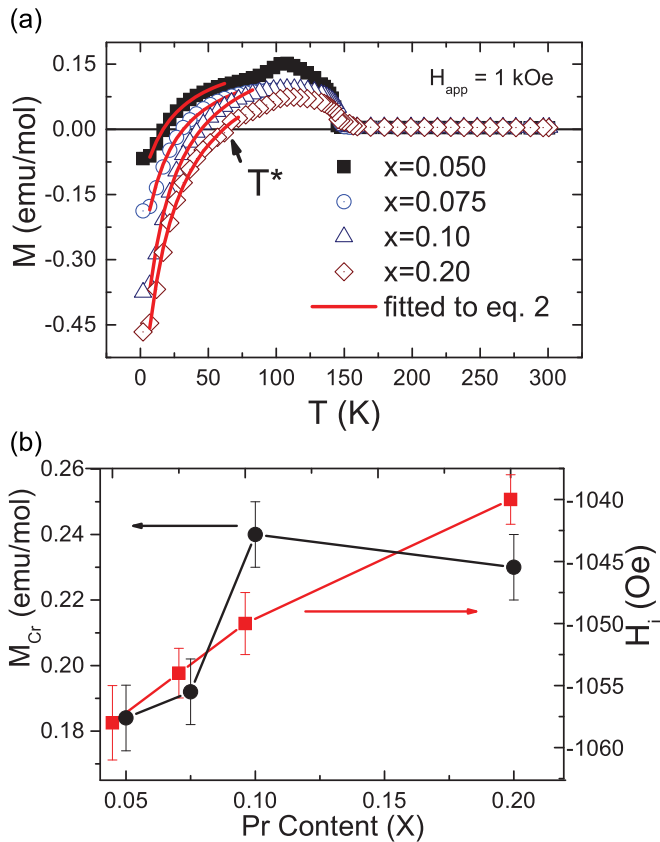


FIG. 10. (a) Susceptibility curves in the FC mode for $Y_{1-x}Pr_xCrO_3$ with $0.050 \leq x \leq 0.20$ content. (b) The Cr magnetization and the H_i obtained from fitting in the same range of composition.

ions plays a crucial role in inducing SR, and (ii) the gradual disappearance of the hysteresis loops when cooling from T_{SR} to lower temperatures (i.e., 50 K) suggests that the spin rotates continuously from T_{SR} down to $T \sim T^*$. Here, from the magnetization results, we infer that the spin reorientation begins at T_{SR} with $\Gamma_4(G_x, A_y, F_z)$ configuration and finishes at $T \sim T^*$ with $\Gamma_1(A_x, G_y, C_z)$ configuration for $x = 0.05, 0.075$, and 0.10 compositions.

The magnetization reversal below T^* is another complex magnetic behavior occurring in $Y_{1-x}Pr_xCrO_3$ between $x = 0.05$ and 0.2 Pr composition. After cooling in an applied magnetic field through T_N (~ 140 K), the Cr^{+3} sublattice imposes an internal field (H_i) affecting the Pr magnetic moments. Figure 10(a) shows the FC measurements over a whole range of temperatures, under an applied field of 1 kOe for $0.05 \leq x \leq 0.20$ samples. As temperature decreases, the FC curves show a maximum and then the diamagnetic signal occurs at T^* . The appearance of H_i can be explained according to the Cooke model [51]. Here, the diamagnetic behavior can be fitted using the following formula:

$$M = M_{Cr} + C_{Pr}(H_i + H_{app})/(T + \Theta). \quad (2)$$

The equation describes the total magnetization of the system assuming two magnetic sublattices, one formed by Cr^{3+} and the other by Pr^{3+} ions. There, M_{Cr} is the saturation magnetization of the Cr^{3+} sublattice, the second term follows the Curie-Weiss law and it is associated with the paramagnetic

contribution of Pr^{3+} ions. The H_i and H_{app} are the internal field and applied magnetic field, respectively. Furthermore, the θ_c is the Weiss temperature and the $C_{Pr} = xC_{exp}$ is attributed to the experimental Curie constant that depends on Pr^{3+} composition, x . The FC curves were fitted at low temperatures, and the fitting range is shown by the solid line in Fig. 10(a). The values of M_{Cr} and H_i as a function of Pr content are plotted in Fig. 10(b). We can see a slight increase of M_{Cr} taking values of 0.18–0.24 emu/mol between 0.075 and 0.1 composition with a slight decrease at 0.22 emu/mol for $x = 0.20$. H_i also slightly decreases from -1058 to -1040 Oe with increasing Pr ion concentration. The values for θ_c are between -20 and -17 K. These results contrast with those obtained in other orthochromite systems; for example, while negative magnetization in $La_{1-x}Pr_xCrO_3$ occurs in a wider range of Pr concentration [34] ($0.2 \leq x \leq 0.8$), in $Y_{1-x}Pr_xCrO_3$ it occurs in a narrower Pr concentration ($0.05 \leq x \leq 0.2$). Furthermore, the M_{Cr} values obtained from fitting at 1 kOe are smaller than those obtained for other homologous compounds. For example, values of 40 emu/mol and $H_i \sim 8500$ Oe were reported in the $La_{0.2}Pr_{0.8}CrO_3$ compound [34]. For $La_{0.5}Gd_{0.5}CrO_3$, magnetization values of 53 emu/mol and $H_i \sim 828$ Oe at 500 Oe were reported [52]. For $NdCr_{1-x}Fe_xO_3$, magnetization values from ~ 7.5 to ~ 23 emu/mol for $0.05 \leq x \leq 0.20$ and 1 kOe were reported [53]. The low magnetization values imply that the ferromagnetic signal from the Cr sublattice is weak below T^* , increasing slightly with Pr^{3+} content. Below T_N , the weak ferromagnetic moments of the Cr sublattice impose a local internal field over the Pr^{3+} moments. In this case, we assume that the Pr moments are randomly distributed at the 4c crystallographic site, namely the long-range ordering of the Pr-Pr sublattice is discarded. Note in Fig. 10(b) that the hysteresis curve for $x = 0.1$ vanishes just before T^* (~ 50 K). At this point, the M_{Cr} contribution is almost zero because the spin rotates from the magnetic configuration to the nonmagnetic configuration, $\Gamma_4(G_x, A_y, F_z) \rightarrow \Gamma_1(A_x, G_y, C_z)$. The induced local internal field ($-H_i$) at the Pr site, under further cooling, exceeds the applied field (H_{app}) just below T^* , so that under an applied field the total magnetization becomes negative since the Pr moments locally increase with decreasing temperature. The result also implies that below T^* , a new AFM spin configuration with a low magnetization ($M_{Cr} \sim 0.20$ emu/mol) takes place due to stronger interaction between magnetic moments of Pr with Cr ions inducing a new magnetic $\Gamma_2(F_x, C_y, G_z)$ configuration. This fact could explain the lower M_{Cr} values obtained from the fitting below of T^* with respect to that reported in other compounds. The ferromagnetic component in the $\Gamma_2(F_x)$ configuration below of T^* in the $Y_{1-x}Pr_xCrO_3$ compound is weaker than that observed in, for example, $GdCrO_3$ where magnetization values, $M_{Cr} = 100$ –400 emu/mol in $\Gamma_4(F_z)$ configuration, were obtained [49,51].

A different situation occurs at lower temperature ($< T^*$). The hysteresis loops show that the nonmagnetic $\Gamma_1(A_x, G_y, C_z)$ configuration is not maintained at 5 K. We observe three important characteristics in the hysteresis curves at 5 K for $Y_{1-x}Pr_xCrO_3$ with $0.025 \leq x \leq 0.3$: (i) the magnetic moment of the Cr^{3+} ions continues to rotate below T^* ; (ii) H_c and M_r show an anomalous behavior for compositions between 0.075 and 0.1 compositions; (iii) negative exchange bias in the

whole range of Pr^{+3} compositions; and (iv) the magnetization and specific-heat curves show an emergence of a peak at 10 K. These results seem to indicate that a new magnetic structure takes place below T^* and the magnetization results are consistent for the coexistence of FM and AFM domains, which explains the exchange-bias effect for $\text{Y}_{1-x}\text{Pr}_x\text{CrO}_3$ for $x = 0.025\text{--}0.30$ composition. Recently, Deng *et al.* [54] performed neutron-diffraction studies on $\text{Y}_{0.9}\text{Pr}_{0.1}\text{CrO}_3$ finding that the $\Gamma_2(F_x, C_y, G_z)$ configuration is dominant and it is associated with the Cr-Cr exchange interaction at 3 K. Here, the hysteresis curves of Fig. 5(d) confirm the development of the $\Gamma_2(F_x, C_y, G_z)$ spin configuration at 5 K, in agreement with the results of Deng *et al.* [54]. The result implies that the $\Gamma_4(G_x, A_y, F_z) \rightarrow \Gamma_1(A_x, G_y, C_z) \rightarrow \Gamma_2(F_x, C_y, G_z)$ spins configuration (Cr^{+3} spin) takes place from T_N to 5 K for $x = 0.075\text{--}0.1$ of Pr^{+3} content. We have mentioned above that the nonmagnetic $\Gamma_1(A_x, G_y, C_z)$ spin configuration takes place at T^* . With further decreasing temperature, the anisotropy of Pr^{+3} ions overcomes that of the Cr^{+3} ions and causes the Cr^{+3} moments to rotate continuously toward the $\Gamma_2(F_x, C_y, G_z)$ spin configuration. It is worthwhile noting two composition regions where the magnetization is controlled by the crystal anisotropy (tilting and octahedral distortion) and the other by a possible short-order Pr-Pr exchange interaction increasing the total magnetization with increasing Pr ion content. To justify these scenarios, we investigate the octahedral distortion effect on the magnetization, taking into consideration H_{EB} values at 5 K as a function of Pr content as is displayed in Fig. 11. A clear tuning of the octahedral distortion and the H_{EB} values from 0.05 to 0.1 of Pr content is observed. There,

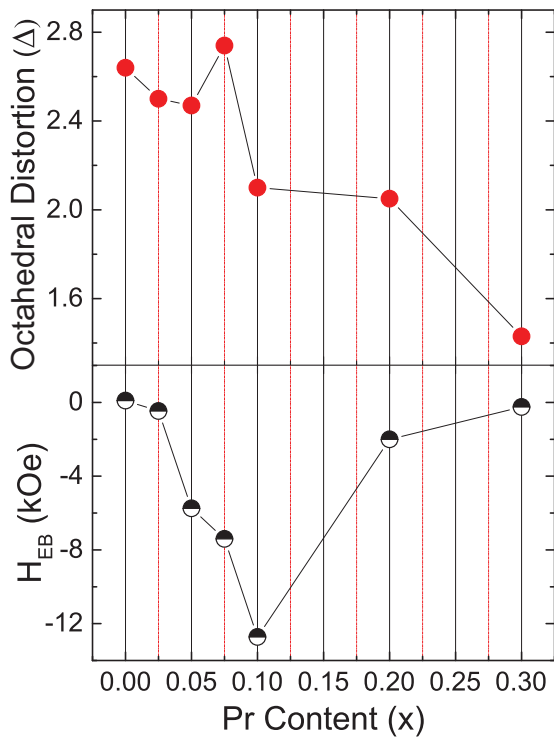


FIG. 11. The octahedral distortion (Δ) behavior at RT is compared with the effective moments in the paramagnetic state (μ_{eff}) and the exchange-bias field (H_{EB}) at 5 K vs Pr content.

a sudden decrease of the octahedral distortion occurring at 0.1 of Pr content accompanied with a maximum in the negative H_{EB} values is observed. Zhou *et al.* [55] showed that the orthorhombic ($Pbnm$ space group) crystalline structure is not rigid and the R substitution causes the cooperative-site rotation inducing an intrinsic octahedral distortion; accordingly, the t - e hybridization should be inevitable. It has been observed that the cooperative-site rotation shifts T_N and the hybridization are the main factors affecting the Cr–O–Cr exchange interaction [56]. Thus, we infer that the t - e hybridization of Cr–O–Cr is modified by the magnetic moment of the Pr ion inducing the anomalous behavior in the octahedral distortion, and thus influencing directly the spin configuration, the magnetization, and the negative exchange-bias effect below T_N , as is clearly seen in Figs. 11(a) and 11(b). This is another important factor that we must not ignore, which also plays an important role in the development of these complex dynamics magnetic phenomena since the octahedral distortion is governed by the octahedral tilting along the [110] and [001] directions, and this, in turn, tunes the magnetic properties. The experimental evidence that supports this fact comes from the magnetic exchange-bias field since these phenomena imply the presence of ferromagnetic domains coexisting with AFM domains, both coming from an independent nature. Note that the strong exchange anisotropy is more visible when the octahedral distortion attains a maximum at 0.1 Pr composition. In other words, the exchange interaction between FM and AFM domains is tuned by octahedral distortion for $0.025 < x < 0.1$, as seen in Fig. 11. On the other hand, the increases in H_c and M_r for higher Pr concentration ($x = 0.2$ and 0.3) should come from another source.

Finally, the development of a peak at 10 K strongly suggests that it is related to the Pr-Pr exchange interaction, which becomes visible at low temperature. For $R\text{CrO}_3$, a second magnetic transition at lower temperatures ($T < T_N$) has been associated with the magnetic R^{+3} ions. The R^{+3} - R^{+3} exchange interaction is the weakest interaction and occurs at $T \leq 10$ K [41]. Several experimental pieces of evidence in the present study predict a new magnetic configuration presumably due to Pr^{+3} ($S = 1$) spins, which could be ferromagnetic. For example, the magnetic contribution to the specific heat showed a peak at about 10 K, increasing continuously as the Pr^{+3} content increased [see the inset in Fig. 8(b)]. Other evidence arises from ZFC magnetization curves [arrows in Figs. 4(c)–4(f)] displaying an incipient peak at about 10 K, which increases in magnitude with increasing Pr content. Thus, for example, it is known that for the PrCrO_3 compound, T_N occurs at ~ 238 K. The spontaneous magnetization of the Cr^{+3} ions is along the [100] direction, taking the $\Gamma_2(F_x, C_y, G_z)$ spin configuration. However, the magnetization data do not show any feature related with the second magnetic transition below 20 K in PrCrO_3 (Refs. [31,43]). On the other hand, neutron-diffraction studies have failed to resolve the second magnetic transition as well as the spin configuration of the Pr-Pr exchange interactions at lower temperatures. Bertaut *et al.* [57] observed spin ordering with a weak ferroelectric component, F_x , above 4.2 K without referring to a Pr magnetic ordering. Afterward, Shamir *et al.* [45] identified a weak magnetic structure ($C_y F_x$ magnetic structure) via neutron-scattering studies at 9 K for the PrCrO_3 compound. Recently, Deng *et al.* [54] performed neutron-diffraction studies in $\text{Y}_{0.9}\text{Pr}_{0.1}\text{CrO}_3$, and they did not

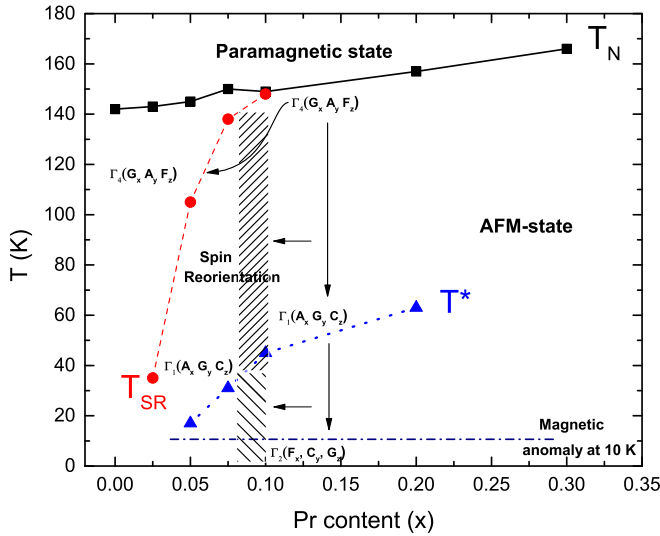


FIG. 12. Phase diagram of $Y_{1-x}Pr_xCrO_3$ ($0 < x < 0.3$). The solid and dashed lines for T_N , T_{SR} , and T^* are guides to the eye. There, T_N , T_{SR} , and T^* denote the Néel, spin reorientation, and compensation temperatures, respectively. The hatched zone denotes the spin dynamic configuration from $\Gamma_4(G_x, A_y, F_z) \rightarrow \Gamma_1(A_x, G_y, C_z) \rightarrow \Gamma_2(F_x, C_y, G_z)$ as a function of temperature.

find signs of magnetic peaks related to the Pr-Pr exchange interaction at 3 K, presumably due to insufficient resolution. However, we discard the assumption of long-range Pr-Pr exchange interaction in the $Y_{1-x}Pr_xCrO_3$ compound since the results in the paramagnetic regime (not shown) did not show an anomaly at about 238 K that indicates a chemical phase separation of the $PrCrO_3$ ($T_N \sim 238$ K) into the $YCrO_3$ ($T_N \sim 142$ K) matrix. This fact also suggests that the Pr ions are chemically disordered in the $4c$ site. Three plausible answers could explain the magnetic behavior at low temperature: (i) the magnetic moments of the Pr ions ($f^2, S = 1$) are frozen, at the crystallographic $4c$ site, inducing spin-glass clusters at about 10 K; (ii) the octahedral distortion promotes the formation of ferromagnetic domains around Pr sites; and (iii) exchange interaction between DM and the single-ion magnetic anisotropy of the Pr ion [53,58]. The DM interaction is responsible for WFM domains, and the single-ion magnetic anisotropy arising from the random magnetic moment of the Pr ion ($4f^2 - S = 1$) could be responsible for the ferromagnetic domains. The net result is an increase of the ferromagnetic domains as Pr increases in the $YCrO_3$ compound.

Based on magnetization and specific-heat results, it was possible to propose a phase diagram that summarizes the main result obtained in $Y_{1-x}Pr_xCrO_3$ ($0 \leq x \leq 0.3$) as seen in Fig. 12. The solid squares represent the Néel temperature and the boundary between the paramagnetic and the AFM state. The solid red circles show the spin-reorientation transition, which is increased from 30 K for $x = 0.025$ to $\sim T_N$ for $x = 0.01$ composition. At lower temperatures, the compensation temperature T^* appears at about 35 K for $x = 0.05$ and increases up to 63 K for $x = 0.20$ (solid blue triangle). At 10 K (dash-dotted line), the magnetic and specific-heat studies show an anomaly that does not change in temperature with increasing Pr^{+3} content and that is presumably due to the

spin freeze of a Pr^{+3} ion. A possible short-range ordering of praseodymium is discarded since there is no evidence of phase separation of $YCrO_3$ and $PrCrO_3$ compounds. In addition, the experimental evidence shows a complex spin-dynamics ground-state configuration below T_N . We found below T_{SR} that the easy magnetization axis rotates continuously from one spin configuration to another at lower temperatures. For example, for $x = 0.10$, the spin reorientation occurs at $T_{SR} \sim 148$ K (hatched zone). There, the $\Gamma_4(G_x, A_y, F_z)$ AFM structure rotates continuously, ending at the $\Gamma_1(A_x, G_y, C_z)$ configuration close to T^* . Afterward, the $\Gamma_1(A_x, G_y, C_z) \rightarrow \Gamma_2(F_x, C_y, G_z)$ spin configuration takes place as is seen by the magnetic hysteresis at 5 K [see Fig. 5(c)]. Recently, Bellaiche *et al.* [7] obtained a simple law that governs the magnetic coupling and takes into account the tilting of the oxygen octahedra (antiferrodistortive quantity, ω_i) and the Dzyaloshinskii-Moriya interaction. The law predicts that the inclination of the octahedrons relaxes the magnetic structure, and thus secondary magnetic orders (such as Γ_1 and Γ_2 spin configurations in this study) can be adopted in order to minimize the total energy.

Though these last assertions are not conclusive, it is worthwhile mentioning that the experimental magnetic behavior as well as the specific-heat studies are a good approach to investigate the spin dynamic induced by temperature; however, a deeper look via neutron-diffraction studies is recommended to confirm the spin ground-state configuration in $Y_{1-x}Pr_xCrO_3$.

V. CONCLUSION

In summary, we present a systematic study of the structure and electronic properties of $YCrO_3$ doped with Pr. We begin from a detailed crystalline characterization followed by studies of the magnetic and thermal properties of $Y_{1-x}Pr_xCrO_3$ with $0 \leq x \leq 0.3$. We found that the magnetic properties are strongly coupled to the structural parameters. Spin reorientation, magnetization reversal, and exchange-bias effects induced by temperature in a short range of Pr composition are a consequence of the competition of antisymmetric (DM) and anisotropic-symmetric exchange interaction between $Pr^{+3} - Cr^{+3}$ ions. It is found that not only are the DM and the single anisotropic ion of Pr magnetic moments responsible for the complex magnetic behavior below T_N , but also the octahedral distortion. The second-order transition of the spin reorientation is dynamic because the easy axis of magnetization rotates beginning at T_{SR} and moving continuously with decreasing temperature, following the $\Gamma_4(G_x, A_y, F_z) \rightarrow \Gamma_1(A_x, G_y, C_z) \rightarrow \Gamma_2(F_x, C_y, G_z)$ spin configuration (Cr spin) from $T_N \rightarrow T^* \rightarrow 5$ K. Furthermore, this fact suggests not only the energetic condition for the presence of both phenomena, but also the development of ferromagnetic domains coexisting with antiferromagnetic domains, both coming from independent sources. The close coexistence of both domains induces the development of the exchange magnetic anisotropy at lower temperatures. There is no signal of a long-range Pr-Pr interaction at low temperature since the Pr ion is randomly distributed in the crystal lattice. However, the magnetization and specific-heat measurements reveal a hump around 10 K, which indicates spin glass of the Pr moments.

ACKNOWLEDGMENTS

A. Durán acknowledges support under Project No. IN103016 (PAPIIT-UNAM), R. Escamilla acknowledges support under Projects No. IN106116/28 (PAPIIT-UNAM) and R. Escudero acknowledges support under Project No. IT100217 (PAPIIT-UNAM). E.V. thanks the Intercambio Académico

UNISON-UNAM (CNYN). Specials thanks to J. Siqueiros for the fruitful comments and for proofreading our manuscript. The technical assistance of P. Casillas, I. Gradilla, E. Aparicio, A. Pompa (IIM), A. López (IIM), and A. Tejada-Cruz (IIM) is acknowledged.

-
- [1] M. B. Salamon and M. Jaime, *Rev. Mod. Phys.* **73**, 583 (2001).
 [2] T. Kimura, T. Goto, H. Shintani, K. Ishizaka, T. Arima, and Y. Tokura, *Nature (London)* **426**, 55 (2003).
 [3] S.-W. Cheong and M. Mostovoy, *Nat. Mater.* **6**, 13 (2007).
 [4] W. Eerenstein, W. D. Mathur, and J. F. Scott, *Nature (London)* **442**, 759 (2006).
 [5] B. Rajeswaran, D. I. Khomskii, A. K. Zvezdin, C. N. R. Rao, and A. Sundaresan, *Phys. Rev. B* **86**, 214409 (2012).
 [6] A. Kumar and S. M. Yusuf, *Phys. Rep.* **556**, 1 (2015).
 [7] L. Bellaiche, Z. Gui, and I. A. Kornev, *J. Phys.: Condens. Matter* **24**, 312201 (2012).
 [8] R. Ramesh and N. A. Spaldin, *Nat. Mater.* **6**, 21 (2007).
 [9] A. B. M. Bibes, *Nat. Mater.* **7**, 425 (2008).
 [10] R. Ramesh, *Nat. Mater.* **9**, 380 (2010).
 [11] J. Prado-Gonjal, R. Schmidt, J. J. Romero, D. Ávila, U. Amador, and E. Morán, *Inorg. Chem.* **52**, 313 (2013).
 [12] T. Yamaguchi and K. Tsushima, *Phys. Rev. B* **8**, 5187 (1973).
 [13] T. Moriya, *Phys. Rev.* **120**, 91 (1960).
 [14] D. Treves, *Phys. Rev.* **125**, 1843 (1962).
 [15] I. A. Sergienko and E. Dagotto, *Phys. Rev. B* **73**, 094434 (2006).
 [16] K. Yoshii and A. Nakamura, *J. Solid State Chem.* **155**, 447 (2000).
 [17] V. A. Khomchenko, I. O. Troyanchuk, R. Szymczak, and H. Szymczak, *J. Mater. Sci.* **43**, 5662 (2008).
 [18] J. Mao, Y. Sui, X. Zhang, Y. Su, X. Wang, Z. Liu, Y. Wang, R. Zhu, Y. Wang, W. Liu, and J. Tang, *Appl. Phys. Lett.* **98**, 192510 (2011).
 [19] E. W. Gorter and J. A. Schulkes, *Phys. Rev.* **90**, 487 (1953).
 [20] R. Pauthenet, *J. Appl. Phys.* **29**, 253 (1958).
 [21] Y. Ren, T. T. M. Palstra, D. I. Khomskii, E. Pellegrin, A. A. Nugroho, A. A. Menovsky, and G. A. Sawatzky, *Nature (London)* **396**, 441 (1998).
 [22] S. I. Ohkoshi, T. Iyoda, A. Fujishima, and K. Hashimoto, *Phys. Rev. B* **56**, 11642 (1997).
 [23] Y. Ren, T. T. M. Palstra, D. I. Khomskii, A. A. Nugroho, A. A. Menovsky, and G. A. Sawatzky, *Phys. Rev. B* **62**, 6577 (2000).
 [24] S. I. Ohkoshi, Y. Abe, A. Fujishima, and K. Hashimoto, *Phys. Rev. Lett.* **82**, 1285 (1999).
 [25] A. Durán, A. M. Arévalo-López, E. Castillo-Martínez, M. García-Guaderrama, E. Moran, M. P. Cruz, F. Fernández, and M. A. Alario-Franco, *J. Solid State Chem.* **183**, 1863 (2010).
 [26] L. Lutterotti, *Nuclear Inst. and Methods in Physics Research B* **268**, 334 (2010).
 [27] R. D. Shannon, *Acta Crystallogr. Sect. A* **32**, 751 (1976).
 [28] A. M. Arévalo-López and M. A. Alario-Franco, *Inorg. Chem.* **48**, 11843 (2009).
 [29] A. Durán, E. Verdin, R. Escamilla, F. Morales, and R. Escudero, *Mater. Chem. Phys.* **133**, 1011 (2012).
 [30] Y. Zhao, D. J. Weidner, J. B. Parise, and D. E. Cox, *Phys. Earth Planet. Inter.* **76**, 17 (1993).
 [31] K. Sardar, M. R. Lees, R. J. Kashtiban, J. Sloan, and R. I. Walton, *Chem. Mater.* **23**, 48 (2011).
 [32] V. M. Jüdin and A. B. Sherman, *Solid State Commun.* **4**, 661 (1966).
 [33] P. Mandal, C. R. Serrao, E. Suard, V. Caignaert, B. Raveau, A. Sundaresan, and C. N. R. Rao, *J. Solid State Chem.* **197**, 408 (2013).
 [34] K. Yoshii, A. Nakamura, Y. Ishii, and Y. Morii, *J. Solid State Chem.* **162**, 84 (2001).
 [35] C. R. Serrao, A. K. Kundu, S. B. Krupanidhi, U. V. Waghmare, and C. N. R. Rao, *Phys. Rev. B* **72**, 220101 (2005).
 [36] J. Nogués and I. K. Schuller, *J. Magn. Magn. Mater.* **192**, 203 (1999).
 [37] I. V. Roshchin, O. Petravic, R. Morales, Z.-P. Li, X. Batlle, and I. K. Schuller, *Europhys. Lett.* **71**, 297 (2005).
 [38] F. Bartolomé, J. Bartolomé, M. Castro, and J. J. Melero, *Phys. Rev. B* **62**, 1058 (2000).
 [39] Y. Sharma, S. Sahoo, W. Perez, S. Mukherjee, R. Gupta, A. Garg, R. Chatterjee, and R. S. Katiyar, *J. Appl. Phys.* **115**, (2014).
 [40] I. S. Jacobs, H. F. Burne, and L. M. Levinson, *J. Appl. Phys.* **42**, 1631 (1971).
 [41] T. Yamaguchi, *J. Phys. Chem. Solids* **35**, 479 (1974).
 [42] E. F. Bertaut, *Acta Crystallogr. Sect. A* **24**, 217 (1968).
 [43] J. D. Gordon, R. M. Hornreich, S. Shtrikman, and B. M. Wanklyn, *Phys. Rev. B* **13**, 3012 (1976).
 [44] R. S. Meltzer, *Phys. Rev. B* **2**, 2398 (1970).
 [45] N. Shamir, H. Shaked, and S. Shtrikman, *Phys. Rev. B* **24**, 6642 (1981).
 [46] R.W. Grant and S. Geller, *Solid State Commun.* **7**, 1291 (1969).
 [47] M. Kaneko, S. Kurita, and K. Tsushima, *J. Phys. C* **10**, 1979 (1977).
 [48] S. Levison, L. M. Luban, and M. Shtrikman, *Phys. Rev.* **187**, 715B (1969).
 [49] K. Yoshii, *J. Solid State Chem.* **159**, 204 (2001).
 [50] K. Yoshii, *Mater. Res. Bull.* **47**, 3243 (2012).
 [51] A. H. Cooke, D. M. Martin, and M. R. Wells, *J. Phys. C* **7**, 3133 (1974).
 [52] N. Sharma, B. K. Srivastava, A. Krishnamurthy, and A. K. Nigam, *Solid State Sci.* **12**, 1464 (2010).
 [53] T. Bora and S. Ravi, *J. Magn. Magn. Mater.* **386**, 85 (2015).
 [54] D. Deng, J. Zheng, D. Yu, B. Wang, D. Sun, M. Avdeev, Z. Feng, C. Jing, B. Lu, W. Ren, S. Cao, and J. Zhang, *Appl. Phys. Lett.* **107**, 102404 (2015).

- [55] J. S. Zhou and J. B. Goodenough, *Phys. Rev. B* **77**, 132104 (2008).
- [56] J. S. Zhou, J. A. Alonso, V. Pomjakushin, J. B. Goodenough, Y. Ren, J.-Q. Yan, and J.-G. Cheng, *Phys. Rev. B* **81**, 214115 (2010).
- [57] E. F. Bertaut, *J. Appl. Phys.* **37**, 1038 (1966).
- [58] S. Dong, K. Yamauchi, S. Yunoki, R. Yu, S. Liang, A. Moreo, J.-M. Liu, S. Picozzi, and E. Dagotto, *Phys. Rev. Lett.* **103**, 127201 (2009).
- [59] J. A. Alonso, M. J. Martínez-Lope, M. T. Casais, and M. T. Fernández-Díaz, *Inorg. Chem.* **39**, 917 (2000).